Journal of Molecular Catalysis A: Chemical 336 (2011) 23–33

Contents lists available at ScienceDirect

Journal of Molecular Catalysis A: Chemical

journal homepage: www.elsevier.com/locate/molcata

Variation of structure and properties of $La_{1-x}Sr_xCo_{0.2}Fe_{0.8}O_{3-\delta}$ with Sr content: Implications for oxidation activity

Nandita Lakshminarayanan [a], John N. Kuhn [a,1], Hyunkyu Choi [a], Jean-Marc M. Millet [b], Umit S. Ozkan [a,*]

[a] The Ohio State University, Department of Chemical and Biomolecular Engineering, Columbus, OH 43210, United States
[b] Institut de Recherches sur la Catalyse et l'Environnement de Lyon, IRCELYON, UMR5256 CNRS-Université Claude Bernard Lyon 1, 2 avenue A. Einstein, F-69626 Villeurbanne cedex, France

ARTICLE INFO

Article history:
Received 19 May 2010
Received in revised form
29 November 2010
Accepted 12 December 2010
Available online 22 December 2010

Keywords:
Perovskite
Solid oxide fuel cell
Oxygen nonstoichiometry
Structure–property
Oxidation activity
Anode catalysts

ABSTRACT

The bulk structure, surface characteristics and catalytic properties of Fe-based perovskite-type oxides with the formula $La_{1-x}Sr_xCo_{0.2}Fe_{0.8}O_{3-\delta}$ for $x = 0.2$, 0.4, 0.6 and 0.8 have been investigated as potential anode catalysts for solid oxide fuel cells. The properties were found to strongly depend upon Sr-content, temperature, and environment. The bulk structure shifted towards being oxygen deficient and cubic under atmospheric conditions as the Sr content increased. The oxygen activation was found to be a strong function of Sr content with the catalysts being more active and having a lower activation energy for Sr-rich $La_{1-x}Sr_xCo_{0.2}Fe_{0.8}O_{3-\delta}$. The materials showed good activity for methane oxidation forming only complete oxidation products and showing no propensity to coke formation, making them a stable potential anode catalyst for SOFCs.

1. Introduction

Perovskite-type (ABO_3) oxide catalysts have been extensively studied over the past several years due to their oxygen storage and conduction properties [1–4]. Their applications include several catalytic reactions including total and partial oxidation reactions of hydrocarbons and volatile organics, photo-catalysis, and environmental applications such as SO_2 removal. They are also widely studied for their use in oxygen sensors and oxygen separation membranes where their anionic conductivity is utilized to achieve high purity separations [5,6]. They have also been studied extensively as potential electrode materials for solid oxide fuel cells, again for their properties related to oxygen activation and conduction [4].

In recent years, there have been several studies on Co- and Fe-based perovskites as potential cathode catalysts. Defect structure and presence of oxygen vacancies can be attributed to the improved oxygen reduction and conduction capabilities in these materials [5]. The activity of these materials is co-limited by bulk ionic transport and the surface exchange kinetics of the oxygen reduction reaction (ORR) [7]. Thus, in these materials both the bulk oxygen pathway as well as the interfacial oxygen reduction kinetics play an important role. It has been shown that surface processes that are chemical in nature such as the surface oxygen exchange and oxygen surface diffusion, influence the performance of mixed conducting perovskite-type materials [5,7–11].

Recently, there has also been increased interest in studying these oxide materials as potential anode catalysts for SOFCs, examining them for their activity for methane oxidation reaction as well as electrochemical performance [12–17]. Replacement of metal-based anodes with redox-stable metal oxides is promising for various reasons, among which is their resistance to coking under most conditions [18]. Moreover the increased ionic conductivity of these materials increases the extent of the triple phase boundary (TPB), which is the electrochemically active region where the oxide ions, the gas phase fuel reactants and the anode reactive sites come into contact. Also, in the case of oxides, the electrode material can be a single component as opposed to cermets, which helps overcome issues such as thermal conductivity mismatches and solid state reactions between the components [19]. However the electrical conductivities of these materials is pretty low which causes poor power densities and cell performances [19]. Studies have proven that the best approach would be to add a functional layer, thus utilizing two different materials for electrical conductivity and the anodic activity [20]. Most of the studies have focused on studying samples with 40% Sr dopant as potential anode materials [21].

* Corresponding author. Tel.: +1 614 292 6623; fax: +1 614 292 3769.
E-mail address: Ozkan.1@osu.edu (U.S. Ozkan).
[1] Present address: University of South Florida, Department of Chemical & Biomedical Engineering, 4202 East Fowler Avenue, ENB 118, Tampa, FL 33620, United States.

1381-1169/$ – see front matter © 2010 Elsevier B.V. All rights reserved.
doi:10.1016/j.molcata.2010.12.006

However based on the properties and activity, this might not be the best candidate. This work focuses on studying the effect of Sr dopant concentration on the properties of doped $LaFeO_3$ catalysts, as well as the effect of the oxygen mobility and oxygen activation properties on the methane oxidation activity.

2. Experimental

2.1. Sample preparation

The $La_{1-x}Sr_xCo_{0.2}Fe_{0.8}O_{3-\delta}$ samples were synthesized using conventional solid-state methods [22]. Metal carbonate and oxide precursors, Co_3O_4 (Aldrich), La_2O_3 (Fisher), Fe_2O_3 (J.T. Baker), and $SrCO_3$ (Alfa Aesar) were used in the synthesis. Stoichiometric proportions of precursors (10 g total) were measured and mixed in a ceramic jar (half pint from U.S. Stoneware) with 1.6–2.5-mm diameter zirconia grinding beads (20 g) and distilled water for 24 h at 120 revolutions per minute using a long roll jar mill (U.S. Stoneware). The mixture was then dried and crushed with a mortar and pestle. It was then calcined at 1000 °C for 48 h (Lindberg Blue tube furnace) in air for the high temperature solid-state reaction to take place and the perovskite structure to form.

2.2. X-ray diffraction

The X-ray powder diffraction patterns were collected using a Bruker D8 Advance diffractometer. The radiation source used was a Cu $K_{\alpha 1}$ radiation source. The instrument is outfitted with an incident beam Ge (1 1 1) monochromator, incident beam Soller slits, and a Braun position sensitive detector (PSD). The current and the voltage were 50 mA and 40 kV. A 9-sample holder using polyethylene holders with a 0.5 mm deep reservoir was used. The scan range was from 2θ values of 20–90° at a step size of 0.0144° and a dwell time of 1 s. Other experimental parameters were as follows: 1° divergence slit, 0.5° anti-scatter slit, and 0.75 detector width. The unit cell parameters were determined using a least-squares fit.

2.3. Temperature-programmed reduction

Temperature-programmed reduction (TPR) studies were conducted with a thermal conductivity detector (TCD) in a house-built system equipped with mass flow controllers. Samples (~85 mg) were loaded into a quartz U-tube reactor with plugs of silica wool and pretreated in 20 sccm/min of 10% O_2/He at 550 °C (10 °C/min) and a hold at the temperature for 20 min in order to clean the surface of adsorbed species and then cooled under the same flow. Reduction was conducted using 30 sccm/min of 10% H_2/N_2, and the temperature was ramped from room temperature to 900 °C. The H_2 consumption was measured using the TCD signal. Calibration was performed by calculating hydrogen consumption necessary to completely reduce CuO and AgO and was used in the quantitative analysis. The calibration was repeated several times to ensure accuracy. Data processing (baseline subtraction and peak integration) was performed using Grams AI software package.

2.4. Thermogravimetric analysis

Thermogravimetric analyses to study oxygen vacancy formation were conducted using a Setaram TG-DSC111 instrument, which is capable of simultaneous microgravimetry as well as calorimetry. Flow balancing was performed in air at 350 °C before each set of experiments. Mass changes associated with thermal changes were determined by blank runs. The sample (~85 mg) was loaded into Pt sample cups. The mass was allowed to equilibrate at room temperature to attain a steady mass before flow was started. The sample was heated to 750 °C at 5 °C/min in 15 sccm/min flow of air and an isothermal hold was conducted for 30 min before being cooled at the same rate. The temperature program was repeated to eliminate the effects of any surface impurities during the first program. The mass change from the second program was then used to calculate the oxygen vacancy formation in the material. The precision of the microbalance is ±1.0 μg, which leads to an accuracy of the oxygen nonstoichiometry ($3-\delta$) to ±0.0002. Reproducibility was checked with four batches of $La_{0.6}Sr_{0.4}Co_{0.2}Fe_{0.8}O_{3-\delta}$, which showed an error margin within 0.001 in the oxygen content calculation.

2.5. Temperature programmed desorption (TPD)

TPD experiments were used to study oxygen vacancy generation in inert atmospheres. Experiments were conducted on both a Thermo-Finnigan Trace Ultra differential scanning quadrupole (DSQ) gas chromatograph/mass spectrometer (GC/MS) and Autochem II 2920 instrument equipped with a Thermal Conductivity Detector (TCD). The TCD signal was calibrated using the instrument's gas calibration feature. Samples (100 mg) were loaded in quartz reactors and were pretreated in 30 sccm/min flow of an oxygen environment (20% O_2/He for GC/MS and 10% O_2/He for Autochem) at 850 °C (10 °C/min) with and hold for 20 min at that temperature. They were then cooled in the same oxygen flows. The flow was then switched to He at 30 sccm/min and the system was purged for 1 h. The TPD was then conducted in He with heating to 900 °C at 10 °C/min and an isothermal hold for 20 min. Data for the GC/MS were obtained using selected ion mode (4, 12, 16, 18, 28, 32, and 44 monitored) and a 3 eV detector gain.

2.6. CO_2 temperature programmed oxidation

CO_2 TPO experiments were performed after first reducing the catalyst with 20 sccm/min of 10% H_2/He at 850 °C for 30 min and cooling it back down to room temperature. The ramp rate was 10 °C/min. The TPO experiment was run with 30 sccm/min of 10% CO_2/He and the sample was heated to 850 °C at 10 °C/min followed by an isothermal hold at 850 °C for 30 min. The effluent gas stream was analyzed using a Cirrus RGA-MS (MKS instruments) used in selected ion mode with a Faraday cup detector.

2.7. Mössbauer spectroscopy

Samples were examined at room temperature by Mössbauer spectroscopy using a conventional constant acceleration spectrometer with 2 GBq ^{57}Co/Rh source. The pulses corresponding to the 14.4 keV photons were accumulated in a 256-channel analyzer and were then sorted according to the velocity of the source varied either in the range of −5 to +5 mm/s or in the range of −10 to +10 mm/s.

Isomer shifts, given with respect to αFe, and quadrupolar splittings were determined within the precision of 0.02 mm/s. The accuracy for hyperfine field calculations was 0.2 T. The peaks positions of the spectra were determined by computer fits using a least-squares minimization assuming Lorenztian line shapes. The areas of the observed signals have been used to evaluate the relative populations of the different iron species, assuming an equal free recoil fraction for all species.

2.8. Transient reaction studies

The temperature programmed reaction experiments were performed with an Autochem II 2920 (Micromeritics) automated catalyst characterization system. The experiments were conducted on an equal surface area (0.92 m^2) basis. Samples were loaded into

U-tube reactors and supported on a plug of quartz wool. The reaction effluent was analyzed by a Cirrus RGA-MS (MKS instruments). This instrument was used in selected ion mode with a electron multiplier detector. The reaction involved a temperature ramp at 10 °C/min from 50 to 700 °C where it was held isothermally for 4 h. The reactant flows for the methane oxidation were 50 sccm/min of 5.0% CH_4/5.0% O_2/He. For experiments with no gas phase oxygen, the feed consisted of 25 sccm/min of 5.0% CH_4/He.

2.9. Steady-state reaction studies

The catalytic tests were performed on an equal surface area (0.92 m^2) basis using a quartz fixed-bed flow reactor. The catalysts were pretreated in 10% O_2/N_2 (50 sccm/min) 850 °C for 20 min and cooled under the same flow. The feed percentages were $CH_4/O_2/N_2$/He = 5/5/40/50 (feed flow rate 50 sccm/min). Nitrogen was used as the internal standard to quantify volumetric flow rate change due to the stoichiometry of the reactions. The reactor effluent was analyzed using a Shimadzu 2014 Gas Chromatograph with a Flame Ionization Detector (FID), Pulse Discharge Helium Ionization Detector (PDHID) and Flame Photometric Detector (FPD). Separations were performed using He as the carrier gas using two columns: Supelco Q Plot (30 m × 0.53 mm, fused silica capillary column) and Carboxen™ 1010 Plot (30 m × 0.53 mm, fused silica capillary column). Reaction data were acquired after waiting at each temperature for steady state to be reached. Conversions and yields are defined as follows:

$$\%\,CH_4\ \text{conversion} = \left(\frac{\text{moles of } CH_4 \text{ converted}}{\text{moles of } CH_4 \text{ in feed}}\right) \times 100$$

$$\%\,O_2\ \text{conversion} = \left(\frac{\text{moles of } O_2 \text{ converted}}{\text{moles of } O_2 \text{ in feed}}\right) \times 100$$

$$\%\,CO_2\ \text{yield} = \left(\frac{\text{moles of } CO_2 \text{ formed}}{\text{moles of } CH_4 \text{ in feed}}\right) \times 100$$

3. Results

3.1. Bulk structure under ambient conditions

The bulk structure of the materials was studied as a function of Sr content using XRD and TPR. The room temperature ambient XRD patterns of the four samples are shown in Figs. 1 and 2. A single-phase perovskite structure is identified in all four cases. The unit cell parameters are obtained over 5 batches of samples and the error bars were calculated from pooled deviations.

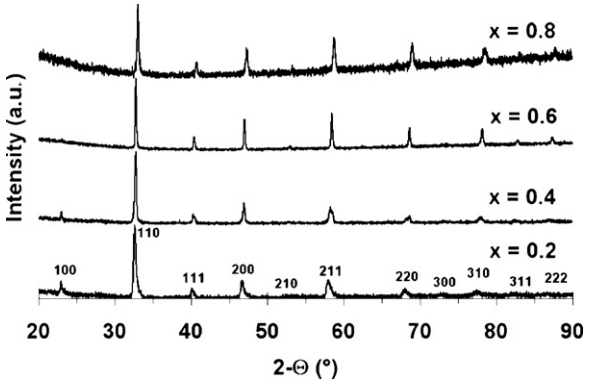

Fig. 1. XRD data for $La_{1-x}Sr_xCo_{0.2}Fe_{0.8}O_{3-\delta}$ under ambient conditions. Data offset for clarity.

As shown in Fig. 3, the unit cell length is found to decrease linearly with increasing Sr content, which is expected as a consequence of replacing more and more of the La atoms in the crystal lattice with smaller Sr atoms. There is also a transition of phase from rhombohedral to cubic symmetry with addition of Sr. The rhombohedral phase approaches the cubic phase as the rhombohedral angle approaches 60°, the value for cubic symmetry. The sample containing 60 and 80% Sr are cubic at room temperature as indicated by a 60° unit cell angle. This is further re-iterated in Fig. 2 where it can be seen that major lines corresponding to the cubic phase all shift towards higher 2θ values indicating a rhombohedral-to-cubic transition with increasing Sr content.

The Mössbauer spectra of the doped $La_{1-x}Sr_xCo_{0.2}Fe_{0.8}O_{3-\delta}$ samples are plotted in Figs. 4 and 5 and the calculated Mössbauer parameters are presented in Table 1. The results obtained are in good agreement with those already published in the literature [23–25]. At 20% Sr content the spectrum is characterized by antiferromagnetic sextuplet with broad lines and a doublet (Fig. 4a). The hyperfine signal (relative intensity 76%) is characterized by an isomer shift of 0.35 mm s^{-1}, typical of octahedrally coordinated Fe^{3+} in high spin configuration. It can better be fitted considering a magnetic fields distribution (Fig. 4b). The existence of such distribution should be related to the presence of the Fe^{4+} cations and to a size distribution of the magnetic domains in relation with a random distribution of the later cations. The doublet (relative intensity 24%) is characterized by a small isomer shift (14 mm s^{-1})

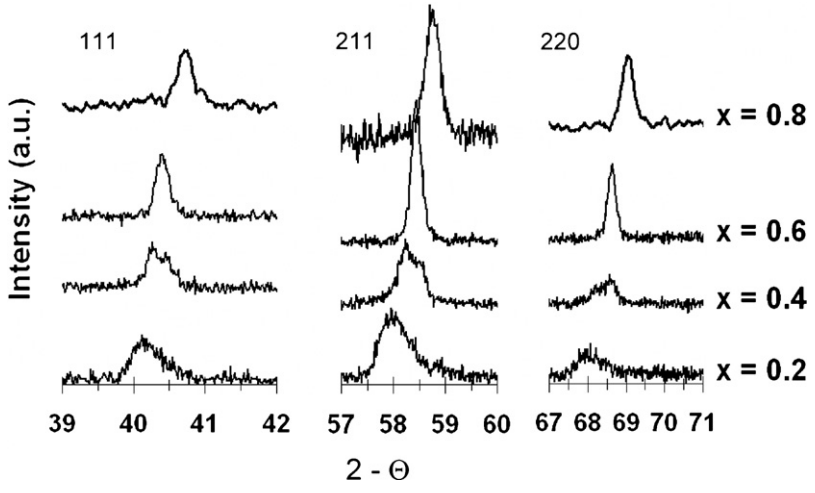

Fig. 2. Cubic Miller Indices (a) 1 1 1, (b) 2 1 1, (c) 2 2 0, and (d) 3 1 0 for $La_{1-x}Sr_xCo_{0.2}Fe_{0.8}O_{3-\delta}$. The data is offset for clarity.

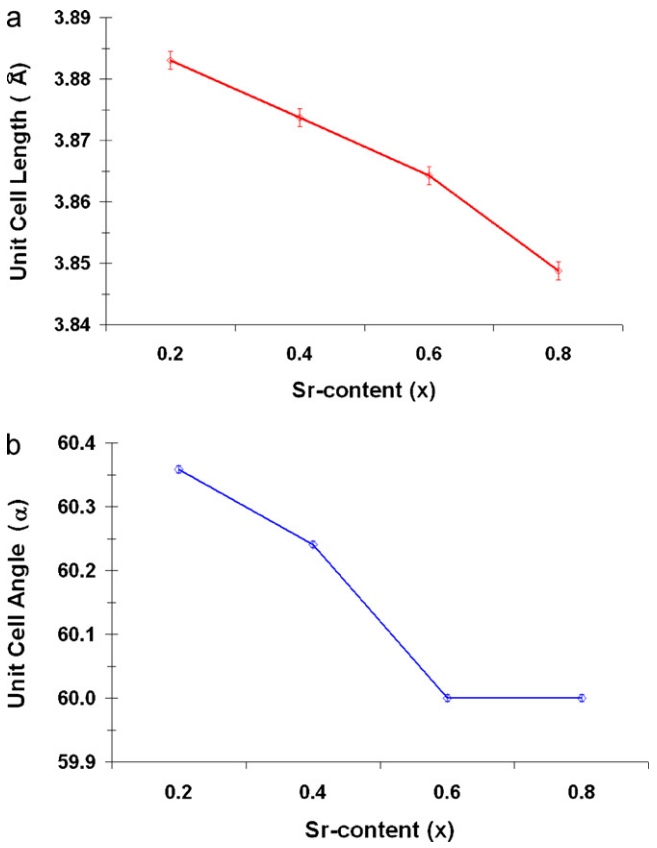

Fig. 3. (a) Unit cell length and (b) angle for $La_{1-x}Sr_xCo_{0.2}Fe_{0.8}O_{3-\delta}$ calculated from ambient XRD results.

and a zero quadrupolar splitting and has been attributed to Fe^{4+} species [26].

At 40, 60 and 80% of Sr dopant concentration, the Mössbauer spectra contain two doublets (Fig. 5). One corresponding to the Fe^{4+} species, already identified in the spectrum of the 20% Sr containing sample, and one corresponding to Fe^{3+} species. A transition from antiferromagnetic to paramagnetic behavior has occurred. The transition is accompanied with a strong decrease of the isomer shift from 0.35 to 0.18 mm s^{-1} as also reported. In general, the relative intensity of the Fe^{4+} doublet increased with the Sr content, but is not directly correlated to the Sr content, which can be explained by the formation of oxygen vacancies to balance the decrease in positive charge.

3.2. Bulk structure as a function of atmosphere

Temperature programmed reduction (TPR) experiments were conducted to study the oxygen content of the samples at ambient conditions, as well as a function of temperature. The H_2 consumption in the TPR is used to calculate the ambient oxygen content of the samples as well as the % of the B-site transition metals in +4 oxidation state. With the replacement of the +3 charged La atoms with Sr (+2) either a corresponding number of the B-site cations move to +4 oxidation state or oxygen vacancies form to maintain electro-neutrality in the sample. Thus, the amount of H_2 consumed to reduce these +4 charged B-site cations can be calculated for a given Sr concentration and subtracted from the total consumption to yield the oxygen content of the original sample. From these calculations, the ambient oxygen content can be deduced and the results are shown in Fig. 6a and b.

It is seen that when there is more La in the sample than Sr, i.e., for Sr dopant concentrations of 0.4 and 0.2, the materials are stoichiometric at room temperature and the percent of tetravalent B-site cations matches the Sr amount. At the higher Sr dopant levels, it can be seen that the increase in the B-site valency alone is insufficient, and the samples become sub-stoichiometric at room temperature. The oxygen vacancy generation with temperature under reducing conditions is also calculated and the results are shown in Fig. 6c. As expected, increasing Sr content leads to larger number of oxygen vacancies at lower temperatures. The percent of tetravalent ions calculated from these TPR studies as well as from the Mössbauer data correlate well as seen in Fig. 7.

Oxygen TPD experiments were also conducted over the samples to study the vacancy evolution under inert atmospheres. The

Table 1
Mössbauer parameters computed from the spectra of the solids, recorded at 25 °C; δ: isomer shift; Δ: quadrupolar splitting; H: internal magnetic field.

Solid	δ (mm s^{-1})	Δ (mm s^{-1})	H (T)	Relative intensity (%)
20	0.35	0.00	47.3[a]	76
	0.14	0.00		24
40	0.18	0.34		61
	0.14	0.00		39
60	0.18	0.28		53
	0.13	0.00		46
80	0.14	0.54		43
	0.08	0.00		57

[a] Mean value of the magnetic fields distribution.

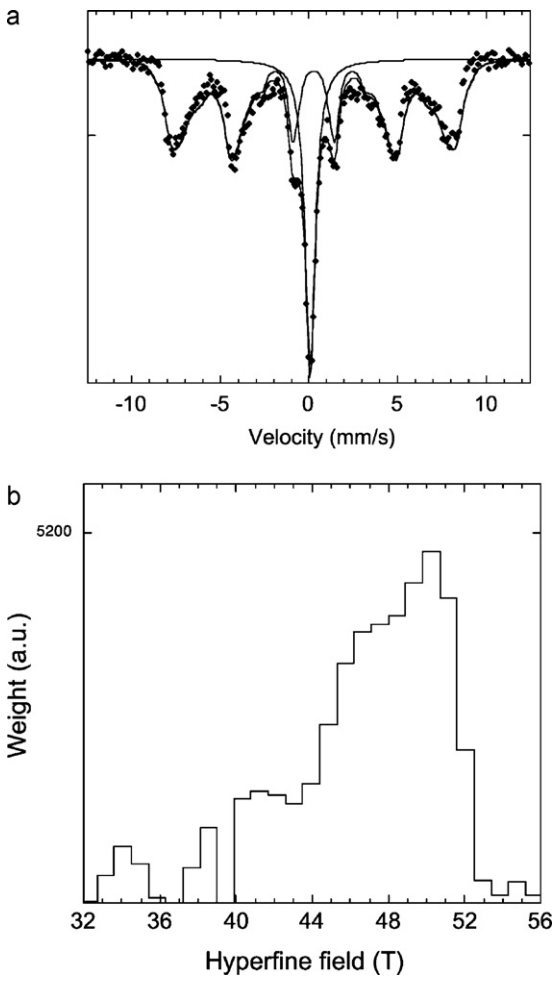

Fig. 4. (a) ^{57}Fe Mössbauer absorption spectra of $La_{0.8}Sr_{0.2}Co_{0.2}Fe_{0.8}O_{3-\delta}$, solid lines are derived from least-square fits; (b) hyperfine field histogram accounting for the magnetic sextet.

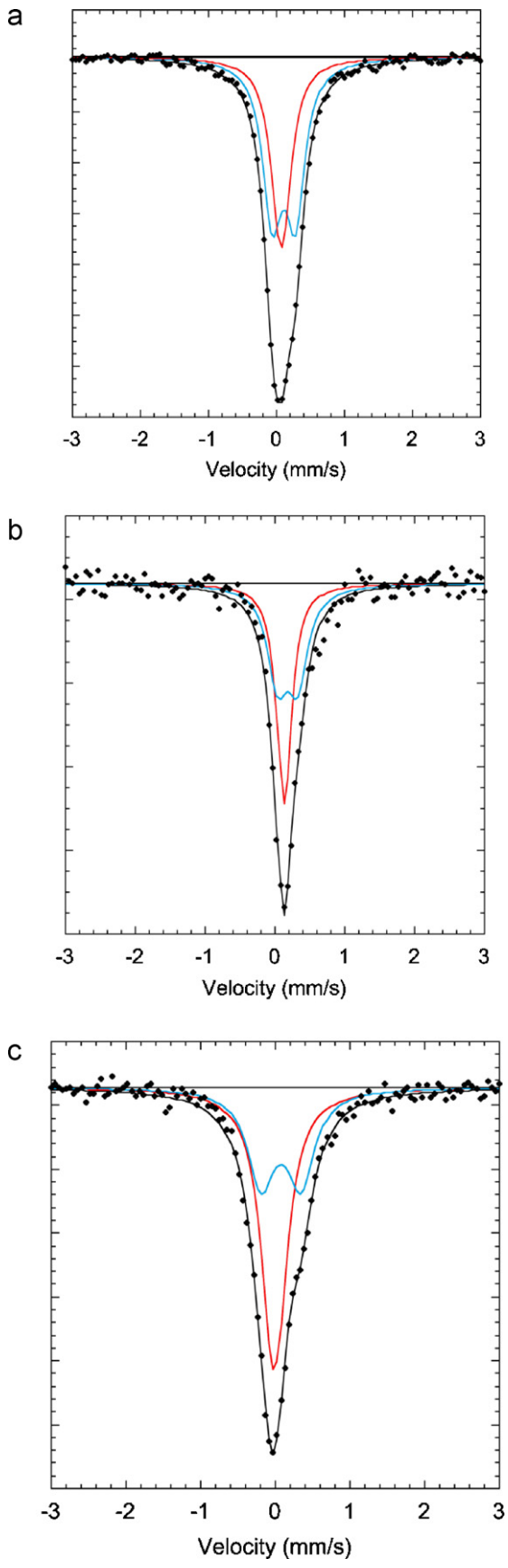

Fig. 5. ^{57}Fe Mössbauer absorption spectra of the $La_{1-x}Sr_xCo_{0.2}Fe_{0.8}O_{3-\delta}$ samples: (a) $x = 0.4$, (b) $x = 0.6$ and (c) $x = 0.8$; solid lines are derived from least-square fits.

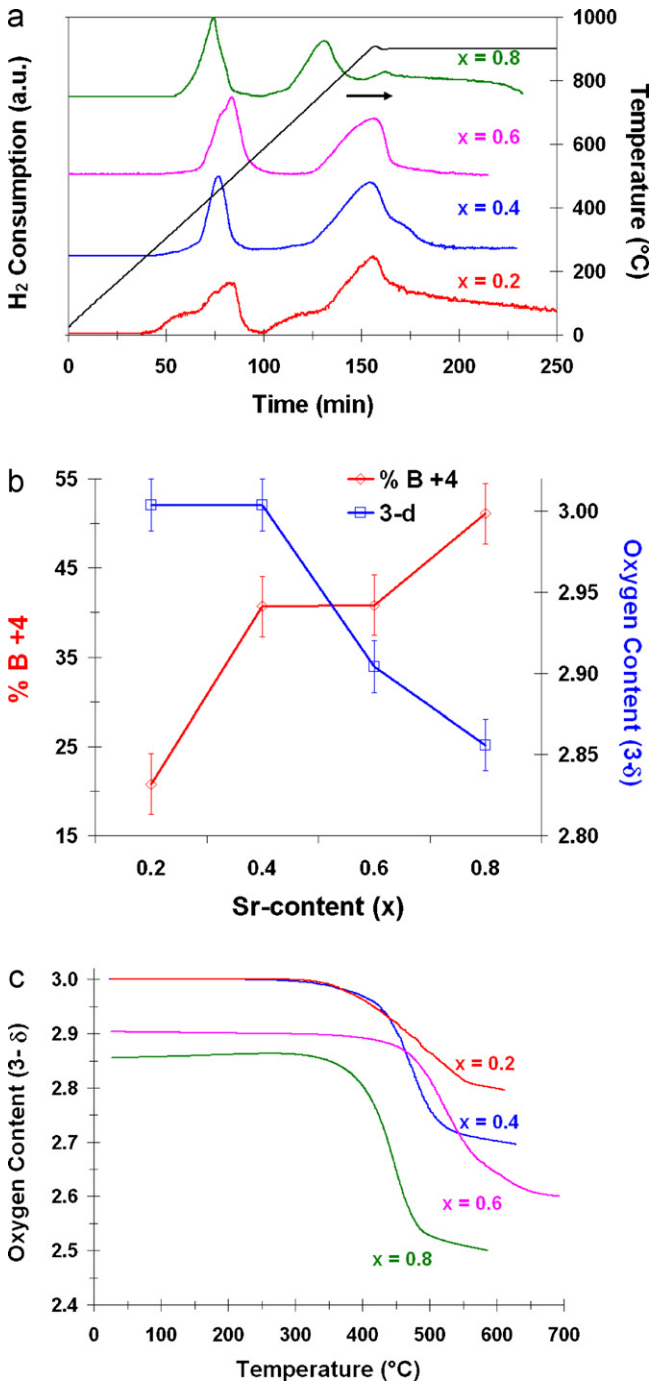

Fig. 6. (a) Temperature-programmed reduction for $La_{1-x}Sr_xCo_{0.2}Fe_{0.8}O_{3-\delta}$ in 10% H_2/N_2 at 10 °C/min ramp rate, (b) ambient oxygen content of $La_{1-x}Sr_xCo_{0.2}Fe_{0.8}O_{3-\delta}$ as a function of Sr doping, and (c) oxygen vacancy generation as a function of temperature.

oxygen evolution was observed and measured using a mass spectrometer and a TCD in two separate experiments using the TPR results as the baseline. From Fig. 8, it is evident that they match each other well. The oxygen evolution from these materials has been studied previously and, in our previous work we have seen a low temperature and a high temperature feature in the oxygen signal [22,27]. The low temperature peak or the α feature is attributed to the reduction of the tetravalent cations, while the high temperature feature or the β is associated with the reduction of the trivalent cations, and is linked to the oxygen mobility in these materials. It can be seen that in general, the β peak increases in size with increas-

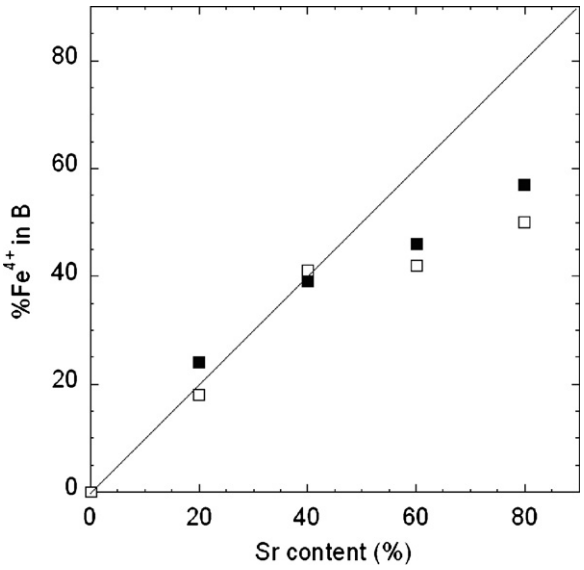

Fig. 7. % of Fe atoms in +4 oxidation state calculated from Mössbauer (□) and TPR (■).

ing Sr content, however, the sample with the highest Sr content shows a dominant low temperature peak, which can be attributed to the increased number of tetravalent B-site ions, and a broad β feature beginning at much lower temperatures. This indicates the ease of reducibility in this sample, especially at lower temperatures.

Thermogravimetric studies were used to study the evolution of oxygen vacancies in air. The results as seen in Fig. 9, using the TPR results as the baseline, again show that the sample with the largest Sr content forms oxygen vacancies with the greatest ease. By comparing the vacancy generation in the three different studies and environments it can be concluded that the vacancies form more readily under reducing and inert conditions when compared to air.

3.3. Surface properties

Surface compositions as a function of dopant concentration were studied using XPS. The spectra for the A- and B-site cations as well as oxygen are shown in Fig. 10. The peaks were deconvoluted and the details are reported in Table 2. In the La 3d region, two different oxidation states for La were identified. A trivalent oxide with the $3d_{5/2}$ peak at 833.3 ev as well as a higher binding energy feature at 837 ev which has been linked to surface hydroxyl groups [28,29]. While there is no significant shift in the peaks, the area decreases as expected with increasing Sr dopant concentration.

Table 2
X-ray photoelectron spectroscopy results summary.

Region	Position (eV)				Surface composition (%)			
	$x=0.2$	$x=0.4$	$x=0.6$	$x=0.8$	$x=0.2$	$x=0.4$	$x=0.6$	$x=0.8$
La 3d	833.3	833.8	833.7	833.6	5.2	2.8	2.8	1.7
	836.9	837.6	837.3	837.3	4.5	2.6	2.7	1.7
Total					9.7	5.4	5.5	3.5
Sr 3d	131.9	132.1	131.7	131.4	1.5	2.8	2.1	4.3
	133.4	133.6	132.6	133.0	2.5	6.9	7.0	5.8
Total					4.0	9.7	9.2	10.0
Co 2p	780.2	781.0	780.8	780.0	1.1	1.0	2.7	1.7
Fe 2p	710.2	710.7	710.4	710.1	7.9	6.7	7.9	7.5
O 1s	528.6	528.3	528.3	529.0	32.3	23.9	14.1	33.8
	531.6	531.7	531.3	531.3	45.1	53.4	60.7	43.5
Total					77.4	77.3	74.9	77.3

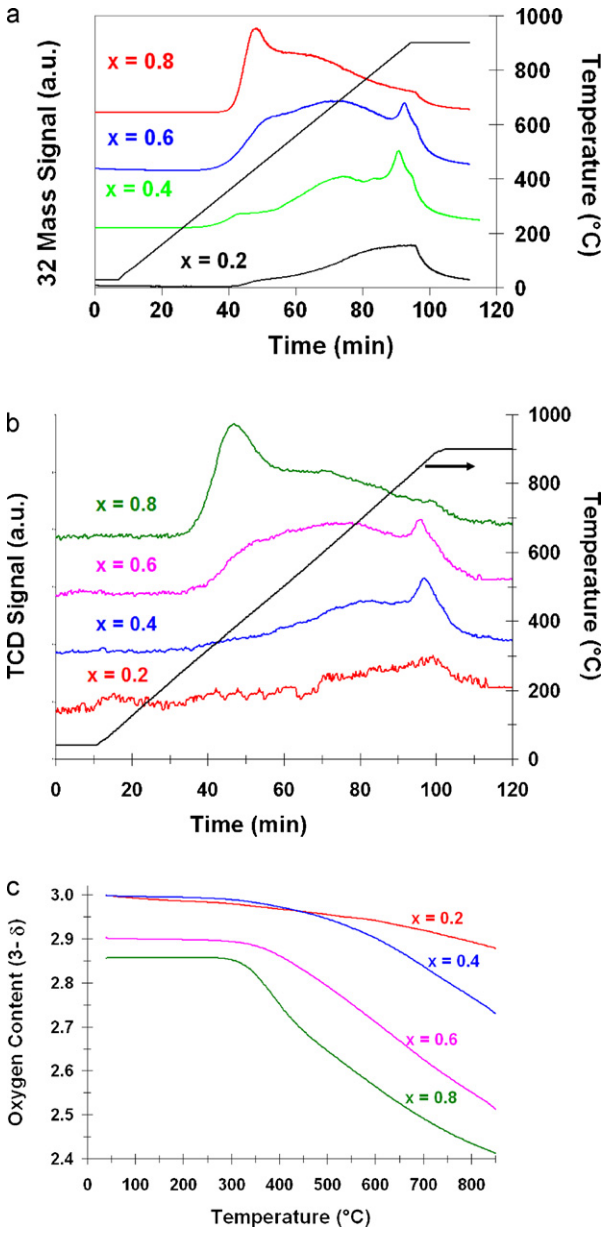

Fig. 8. Oxygen TPD profiles for $La_{1-x}Sr_xCo_{0.2}Fe_{0.8}O_{3-\delta}$ acquired by (a) MS and (b) TCD. Data is offset for clarity. (c) Oxygen vacancies from calibrated TCD signal.

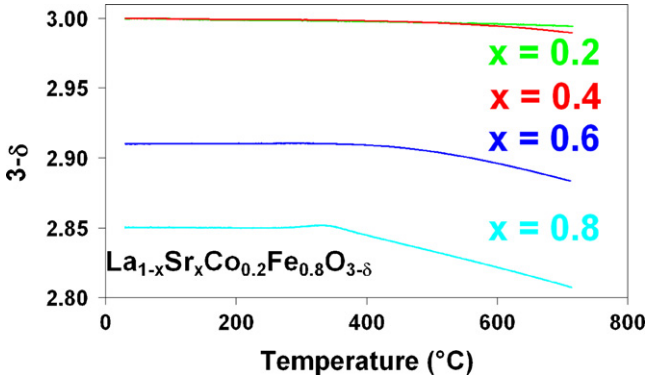

Fig. 9. Oxygen vacancy generation in air measured by TGA-DSC.

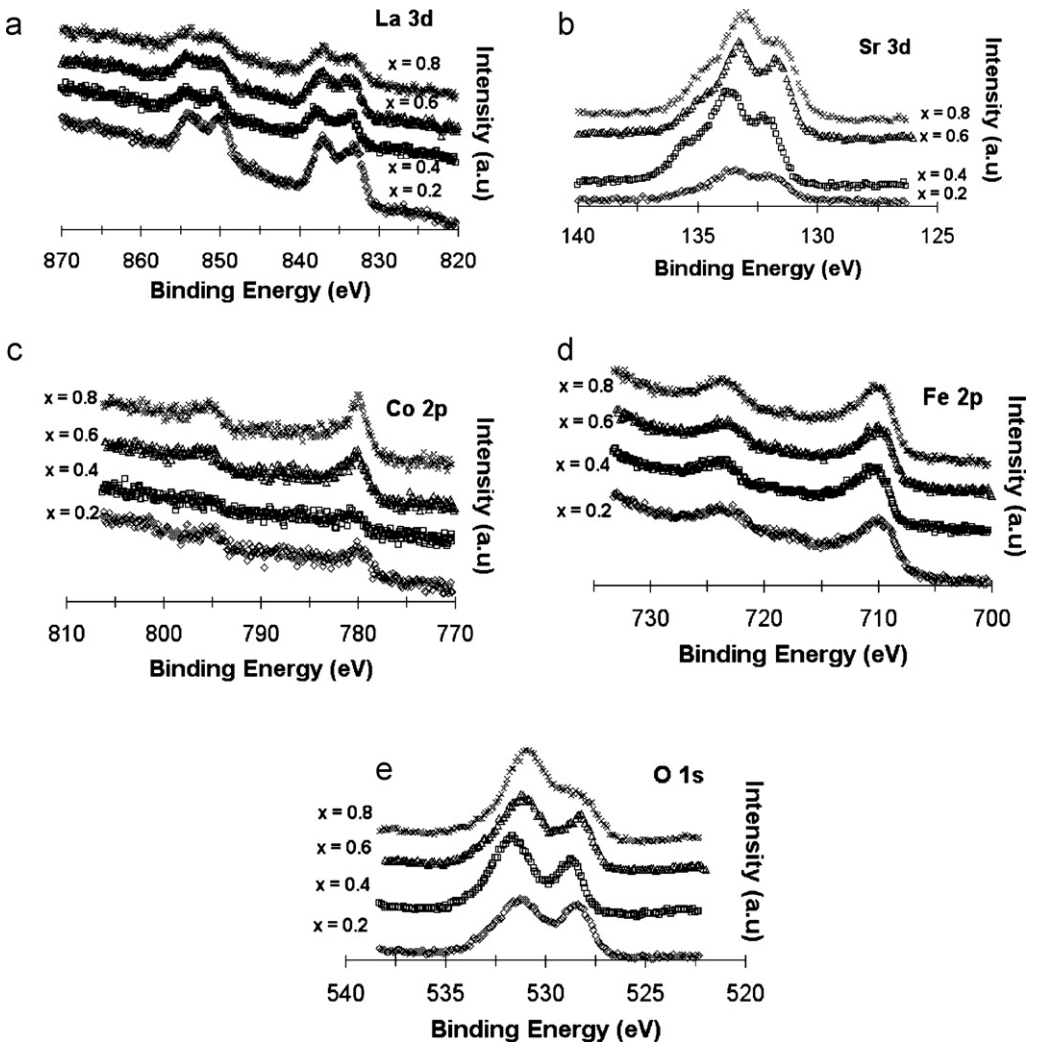

Fig. 10. X-ray photoelectron spectra for $La_{1-x}Sr_xCo_{0.2}Fe_{0.8}O_{3-\delta}$.

In the Sr 3d region, we see two peaks associated with SrO (133 eV) as well a sub-oxide species (131.5 eV) at lower binding energies [29]. The concentration of these two species on the surface increases steadily with increasing Sr content. The oxygen 1s region showed interesting shifts with increasing Sr content. While the higher binding energy peak corresponds to chemisorbed oxygen, the lower binding energy peak is attributed to oxide ions in the lattice. Looking at the overall composition of the surface as indicated by the percentage values in Table 2, it appears that the surface is enriched in oxygen as compared to the bulk. With increase in the Sr doping level, it is seen that the lower binding energy oxygen peak decreases in size and follows a similar trend to the TPD data discussed in the previous section, wherein at higher Sr dopant levels, the sample is sub-stoichiometric in oxygen at room temperature. The Fe 2p region shows a band wide enough to include contributions from Fe in +4 (712 eV) and +3 (710 eV) oxidation states.

3.4. CO_2 temperature programmed oxidation (TPO)

CO_2 TPO has been used before to study oxygen mobility over perovskite oxides [30]. The mechanism of CO_2 dissociation and CO evolution involves formation of surface oxygen species, which then need to be interfacially transported into the lattice. Thus activity for the CO_2 reduction/dissociation is a good indicator of the rate at which surface oxygen moves into the lattice. It is commonly known that the oxygen reduction reaction at the SOFC cathode is co-limited by both surface reaction as well as the interfacial transport [7]. Fig. 11 shows the $m/z = 28$ (CO evolution) signals from the CO_2 TPO experiments obtained over pre-reduced catalysts. It is seen that there are two distinct features in the TPO,

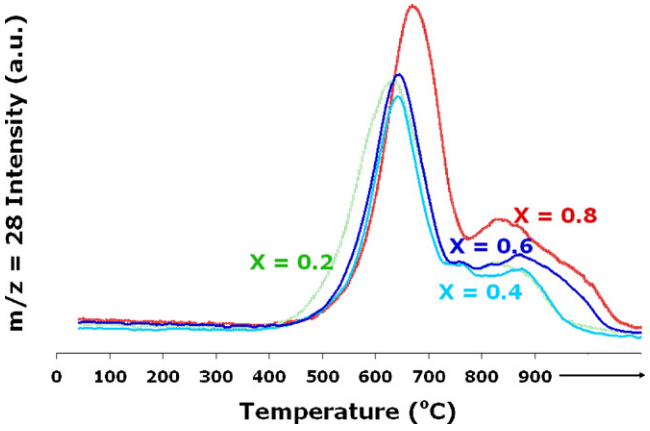

Fig. 11. CO_2 temperature programmed oxidation over $La_{1-x}Sr_xCo_{0.2}Fe_{0.8}O_{3-\delta}$.

a sharp low temperature peak at around 600 °C and a broad shoulder at higher temperature at around 800 °C. These features can be attributed to different oxygen sites and vacancies in the catalyst surface and bulk. Both features increase in intensity with increasing Sr content. The oxygen TPD results (Fig. 8) also showed two peaks attributed to different redox couples in the catalyst. The mechanism of the CO_2 TPO is said to involve oxygen vacancies in the lattice and the two features we see in the CO_2 evolution are possibly associated with different lattice sites. The high temperature feature involves the sites that are harder to re-oxidize and these sites become more accessible for the TPO with increasing oxygen content due to increased oxygen mobility. Although there are differences in the CO_2 evolution intensity as well as temperature as a function of the Sr doping level, the sample with the highest Sr doping shows the most pronounced increase in CO_2 dissociation.

3.5. Reaction activity

Methane oxidation activity of the catalysts was studied as a function of Sr dopant level over the $La_{1-x}Sr_xCo_{0.2}Fe_{0.8}O_{3-\delta}$ catalysts using both transient and steady state experiments. The results from the transient Temperature Programmed Reaction (TPRxn) experiments are shown in Fig. 12. The signals are normalized in order to view the features better. CO_2 and H_2O were the primary products of oxidation over all catalysts. Also, partial oxidation products such as CO were not observed in any case. The methane conversion takes off over all catalysts at around 400 °C. The oxygen conversion and CO_2 light-off temperatures are also around 400 °C. At lower temperatures before reaction takes off, we see a peak in the oxygen signal, indicating desorption of oxygen from the catalyst. The extent of desorption increases with increasing Sr content. At the lower dopant concentrations, there is almost no desorption. When methane conversion takes off close to 400 °C, we see drops in the 32 signal with a corresponding rise in the CO_2 signal. Oxygen is the limiting reactant in these reactions as the feed contains sub-stoichiometric oxygen. In all cases, there is a local maximum in the CO_2 signal and a local minimum in the methane signal, and this is due to the oxygen desorption from the lattice. The size of the maxima and minima is a function of the Sr dopant concentration. At higher temperatures, the gas phase oxygen and the surface oxygen vacancies eventually equilibrate to reach a steady activity, and CO_2 and methane signals reach constant values determined by the oxygen concentration in the feed. At this point, the oxygen signal is zero.

In order to study this effect further, another methane oxidation experiment where no gas phase oxygen was supplied to the system was conducted. In this case, the partial oxidation products, H_2 and CO are the primary products of reaction. The 28 signal from the experiment is shown in Fig. 13. A window of activity is observed for the methane oxidation to CO and H_2. In all cases, onset of activity takes place at around 650 °C and there are multiple peaks corresponding to different oxygen sites in the lattice. The temperature window of activity extends to much higher temperatures with increasing Sr dopant concentrations. For the sample with 80% Sr, it is seen that the largest feature is observed at 800 °C. Also, the lower temperature features are comparable in area to the sample with lower Sr content. Comparing the overall CO evolution from the sample it is observed that it is a linear function of the Sr content. With increasing Sr content, we see that more oxygen in the sample lattice becomes available for the oxidation reaction. This implies that there is increased oxygen mobility in the samples with higher oxygen content, which facilitates higher methane oxidation activity.

Steady-state activity was also studied for methane oxidation. As seen in the transient experiments, for these feed conditions, CO_2 and H_2O were the favored products of oxidation, although small

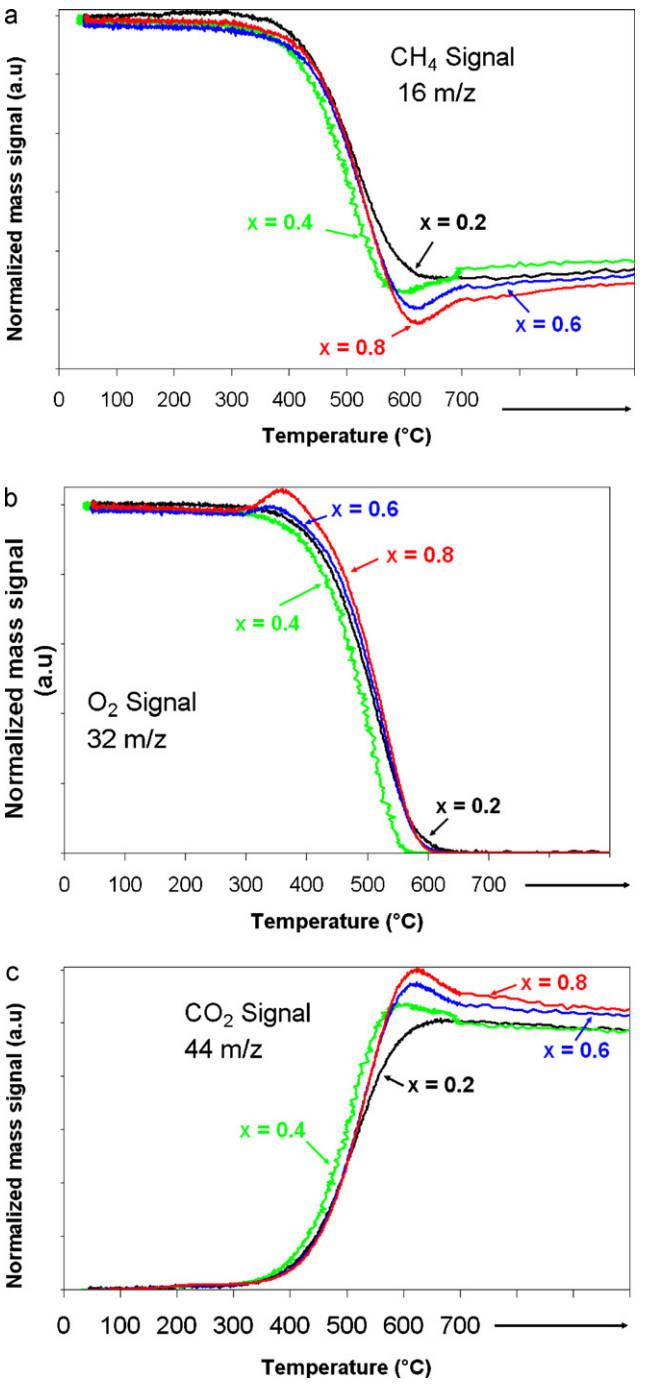

Fig. 12. TPRxn: methane oxidation over $La_{1-x}Sr_xCo_{0.2}Fe_{0.8}O_{3-\delta}$: (a) Methane, (b) O_2 and (c) CO_2 signals.

amounts of CO and H_2 were also observed (less than 1% yield). The CO_2 yields and oxygen conversions are presented in Fig. 14a and b, respectively. Complete oxygen conversion was reached over all catalysts by 550 °C. The feed was sub-stoichiometric in oxygen, and hence the maximum methane conversion and CO_2 yield was limited by the availability of oxygen. At lower temperatures, we see that the samples with the higher Sr dopant levels show a higher oxygen conversion than the La-rich catalysts. This can be attributed to increased oxygen mobility in these samples, due to increased oxygen vacancy formation and hence higher oxygen activation. Apparent oxygen activation energies calculated from an Arrhenius plot shown in Fig. 14c are tabulated in Table 3. We see a significant decrease in activation energies with increasing Sr con-

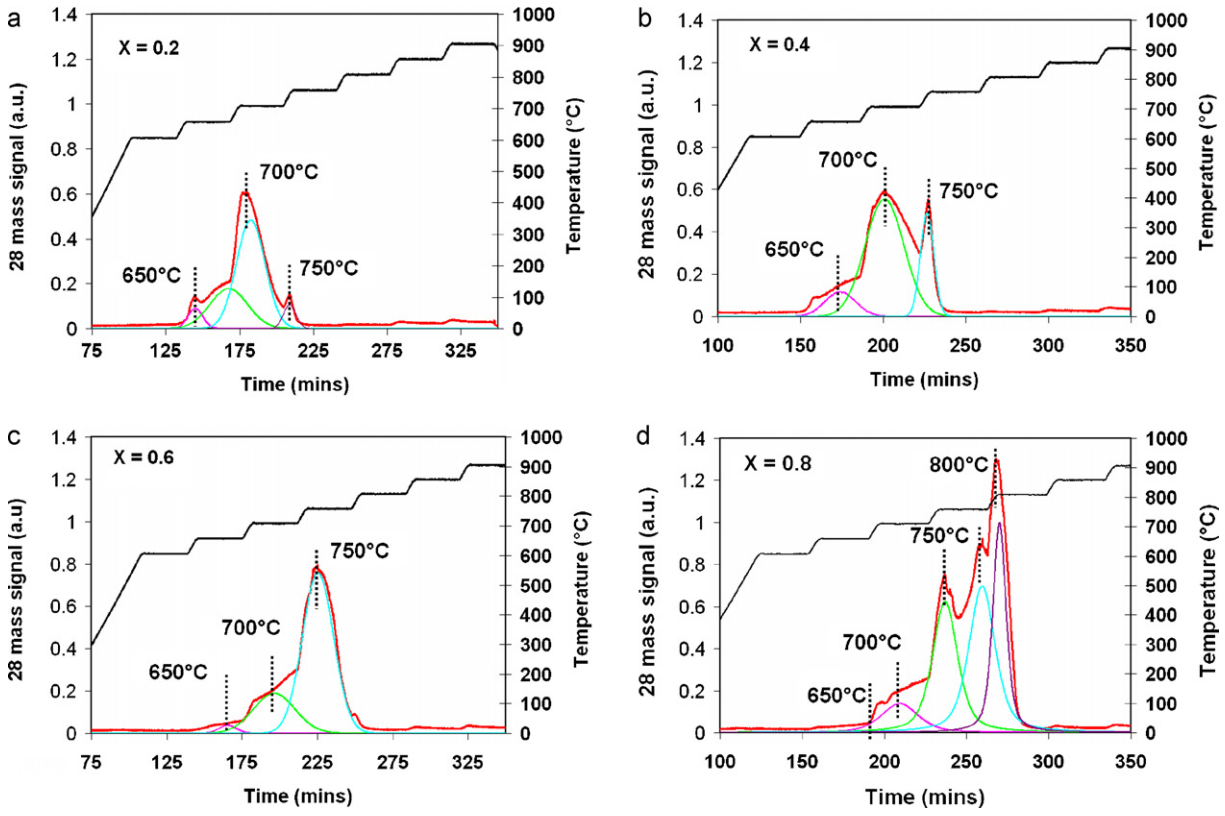

Fig. 13. TPRxn: Methane Oxidation with lattice oxygen: CO signal for $La_{1-x}Sr_xCo_{0.2}Fe_{0.8}O_{3-\delta}$ (a) $x = 0.2$ (b) $x = 0.4$ (c) $x = 0.6$ (d) $x = 0.8$.

tent. The oxygen vacancies as well as increased oxygen mobility in these materials improve surface oxygen activation.

4. Discussion

4.1. Effect of Sr content on bulk structure and properties

The effect of Sr doping on the bulk and surface properties of $La_{1-x}Sr_xCo_{0.2}Fe_{0.8}O_{3-\delta}$ has been studied using a variety of techniques. The formation of vacancies and oxygen stoichiometry, which are strong functions of the dopant concentration, affect the unit cell symmetry, bulk and surface elemental concentrations. The samples where the Sr content was 60% and above, were observed to be non-stoichiometric with respect to oxygen even at room temperature. A rhombohedral-to-cubic symmetry transition is observed in Sr-rich samples. In general, a cubic structure being more symmetric is expected to lead to higher anionic conductivity. The level of symmetry in perovskite-type structures has been shown to influence performance [31–34,6]. The oxygen stoichiometry is also a strong function of environment, with greater oxygen vacancies forming under reducing conditions compared to that in air. This makes it an interesting material as an SOFC anode catalyst also.

Table 3
Oxygen activation energies from steady-state methane oxidation on $La_{1-x}Sr_xCo_{0.2}Fe_{0.8}O_{3-\delta}$.

X	E_a (kJ/mol)
0.2	128
0.4	121
0.6	70
0.8	57

4.2. Oxygen mobility and oxidation activity

The samples showed good activity for the methane oxidation reaction and only complete oxidation products were observed. Most of the studies that included methane oxidation over these materials have been conducted under conditions of excess oxygen [35–37]. In our studies, oxygen served as the limiting reactant, and reaction tests were performed under these conditions to simulate conditions in an SOFC anode, where the supply of oxygen is limited by the rate at which it is conducted through the electrolyte to the anode. Operating at these conditions provided good in-sight into the differences in oxygen and methane activation as a function of temperature and Sr content in these samples. It is established in the literature that the oxidation of methane over perovskite oxides takes place through an interfacial process where the lattice oxygen is the source of the active oxygen involved in the reaction. A Mars–Van Krevelen redox cycle is involved, wherein the bulk oxygen migrates to the surface and is involved in the oxidation of the surface adsorbate, while it is replaced in bulk by the gas phase oxygen [3,37]. Thus the mobility of the oxide ions within the bulk plays a vital role in the catalysis mechanism. This difference in mobility is more apparent under limiting oxygen conditions. We observe increased oxygen activation and methane oxidation activity at lower temperatures with the higher Sr content and oxygen mobility. At higher temperatures we see the activity go through a maxima as the bulk oxygen content of the sample equilibrates. This is further explained by the results observed, as shown in Fig. 13, when the oxidation is carried out with no external oxygen feed. These results are further put into context by other studies where the methane oxidation selectivity was found to be a strong function of lattice oxygen content [38]. Thus, experiments in limited oxygen can be useful in studying the catalytic activity of these materials as potential SOFC anodes. It is known that increasing Sr content in these materials increases the thermal expansion coefficient (TEC)

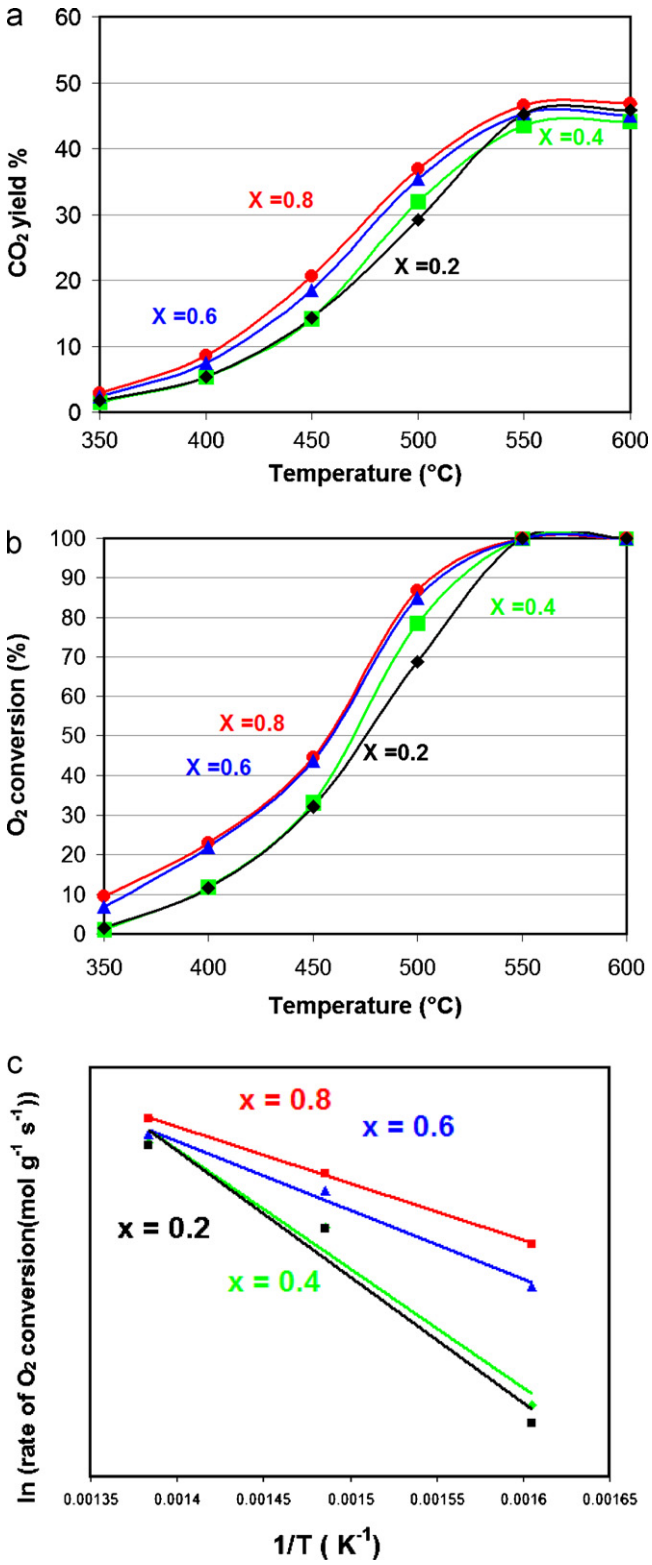

Fig. 14. Steady-state methane oxidation over $La_{1-x}Sr_xCo_{0.2}Fe_{0.8}O_{3-\delta}$. (a) CO_2 yield, (b) oxygen conversion and (c) Arrhenius calculations.

of these materials significantly over that of Yttria-Stabilized Zirconia, which is the state of the art electrolyte material in solid oxide fuel cells. However, the TEC can be controlled with method of synthesis as well as pretreatment parameters [4]. It is important to optimize the composition for maximum activity as well as compatibility.

5. Conclusions

The bulk structure and surface properties of $La_{1-x}Sr_xCo_{0.2}Fe_{0.8}O_{3-\delta}$ for $x = 0.2$, 0.4, 0.6 and 0.8, have been studied as a function of Sr content and environment. The oxygen nonstoichiometry, which is an important property determining anionic conductivity, mobility and oxygen activation, was studied using several characterization tools. The correlation with oxygen activation and oxygen mobility of the sample was studied using methane oxidation under rich-burn conditions as a model reaction system. Significant differences were observed between the samples for oxidation activity at lower temperatures. Catalyst with the higher Sr dopant concentration showed greater degree of oxygen activation at lower temperatures. These results may have important implications in identifying optimum Sr contents for using these materials as anode or oxidation catalysts.

Acknowledgments

The financial support provided for this work by the Ohio Coal Development Office and the Ohio Department of Development through a Wright Center of Innovation is gratefully acknowledged. The authors would also like to acknowledge NSF support for acquisition of the XPS system under NSF-DMR grant #0114098.

References

[1] L.G. Tejuca, J.L.G. Fierro, J.M. Tascon, Advances in Catalysis 36 (1989) 237.
[2] M.A. Pena, J.L.G. Fierro, Chemical Reviews 101 (2001) 1981.
[3] L.G. Tejuca, J.L.G. Fierro (Eds.), Properties and Applications of Perovskite-type Oxides, Marcel Dekker, Inc., New York, 1993.
[4] R.M. Ormerod, Chemical Society Reviews 32 (2003).
[5] H.J.M. Bouwmeester, H. Kruidhof, A.J. Burggraaf, Solid State Ionics 72 (1994) 185.
[6] J.F. Vente, S. McIntosh, W.G. Haije, H.J.M. Bouwmeester, Journal of the Electrochemistry Society 10 (2006) 581.
[7] S.B. Adler, Chemical Reviews 104 (2004) 4791.
[8] B.C.H. Steele, Solid State Ionics 94 (1997) 239.
[9] S.B. Adler, Solid State Ionics 111 (1998) 125.
[10] S.B. Adler, Solid State Ionics 135 (2000) 603.
[11] S.B. Adler, J.A. Lane, B.C.H. Steele, Journal of the Electrochemistry Society 143 (11) (1996) 3554.
[12] D.P. Fagg, J.T.S. Irvine, Journal of Materials Chemistry 7 (12) (1997) 2495–2498.
[13] A.L. Sauvet, J.T.S. Irvine, Solid State Ionics 167 (1–2) (2004) 1–8.
[14] S. Tao, J.T.S. Irvine, Chemistry of Materials 16 (21) (2004) 4116–4121.
[15] E.S. Putna, J. Stubenrauch, J.M. Vohs, R.J. Gorte, Langmuir (1995) 4832–4837.
[16] G. Pudmich, B.A. Boukamp, M. Gonzalez-Cuenca, W. Jungen, W. Zipprich, F. Tietz, Solid State Ionics 135 (1–4) (2000) 433–438.
[17] B.D. Madsen, S.A. Barnett, Journal of the Electrochemistry Society 154 (6) (2007) pB501.
[18] R.J. Gorte, J.M. Vohs, Journal of Catalysis 216 (1–2) (2003) 477–486.
[19] S. McIntosh, R.J. Gorte, Chemical Reviews 104 (2004) 4845–4865.
[20] S. Tao, J.T.S. Irvine, The Chemical Record 4 (2004) 83–95.
[21] A. Hartley, M. Sahibzada, M. Weston, I.S. Metcalfe, D. Mantzavinos, Catalysis Today 55 (2000) p197.
[22] J.N. Kuhn, U.S. Ozkan, Catalysis Letters 121 (3–4) (2008) 179–188.
[23] A. Delmastro, D. Mazza, S. Ronchetti, M. Vallino, R. Spinicci, P. Brovetto, M. Salis, Materials Science and Engineering: B 79 (2) (2001) 140–145.
[24] U. Russo, L. Nodari, M. Faticanti, V. Kuncser, G. Filoti, Solid State Ionics 176 (1–2) (2005) 97–102.
[25] J.N. Kuhn, P.H. Matter, J.-M.M. Millet, R.B. Watson, U.S. Ozkan, The Journal of Physical Chemistry C 112 (32) (2008) 12468–12476.
[26] E. Fluck, W. Kerler, W. Neuwirth, Angewandte Chemie International Edition 2 (1963) 277–287.
[27] T. Seiyama, N. Yamazoe, K. Eguchi, Industrial and Engineering Chemistry Product Research and Development 24 (1985) p19.
[28] M. Machkova, N. Brashkova, P. Ivanov, J.B. Carda, V. Kozhukharov, Applied Surface Science 119 (1–2) (1997) 127–136.
[29] J.N. Kuhn, U.S. Ozkan, Journal of Catalysis 253 (1) (2008) 200–211.
[30] T.-J. Huang, X.-D. Shen, C.-L. Chou, Journal of Power Sources 187 (2) (2009) 348–355.
[31] K. Wiik, S. Aasland, H.L. Hansen, I.L. Tangen, R. Ødegard, Solid State Ionics 152–153 (2002) 675.

[32] L. Qui, T.H. Lee, L.M. Liu, Y.L. Yang, A.J. Jacobson, Solid State Ionics 76 (1995) 321.
[33] H. Kruidhof, H.J.M. Bouwmeester, R.H.E. v. Doorn, A.J. Burggraaf, Solid State Ionics 63–65 (1993) 816.
[34] S. McIntosh, J.F. Vente, W.G. Haije, D.H.A. Blank, H.J.M. Bouwmeester, Solid State Ionics 177 (2006) 833.
[35] S. Royer, H. Alamdari, D. Duprez, S. Kaliaguine, Applied Catalysis B: Environmental 58 (2005) 272.
[36] S. Royer, F. Berube, S. Kaliaguine, Applied Catalysis A: General 282 (2005) 273.
[37] L. Forni, I. Rossetti, Applied Catalysis B: Environmental 38 (2002) 29.
[38] M. van den Bossche, S. McIntosh, Journal of Catalysis 255 (2) (2008) 313–323.